The Astrophysical Journal, 973:147 (10pp), 2024 October 1 https://doi.org/10.3847/1538-4357/ad6840

Spindown of Pulsars Interacting with Companion Winds: The Impact of Magnetospheric Compression

Yici Zhong[1,2], Anatoly Spitkovsky[2], Jens F. Mahlmann[3], and Hayk Hakobyan[3,4]
[1] Department of Physics, Graduate School of Science, University of Tokyo, Bunkyo-ku, Tokyo 113-0033, Japan; yici.zhong@phys.s.u-tokyo.ac.jp
[2] Department of Astrophysical Sciences, Peyton Hall, Princeton University, Princeton, NJ 08544, USA
[3] Physics Department & Columbia Astrophysics Laboratory, Columbia University, New York, NY 10027, USA
[4] Computational Sciences Department, Princeton Plasma Physics Laboratory (PPPL), Princeton, NJ 08540, USA
Received 2024 July 10; revised 2024 July 26; accepted 2024 July 26; published 2024 September 27

Abstract

Pulsars in binary systems with strong companion winds can have the magnetopause separating their magnetosphere from the wind located well within their light cylinder. This bow-like enclosure effectively creates a waveguide that confines the pulsar's electromagnetic fields and can significantly alter its spindown. In this paper, we study the spindown of compressed pulsar magnetospheres in such systems. We parameterize the confinement as the ratio between the equatorial position of the magnetopause (or standoff distance) $R_{\rm m}$ and the pulsar's light cylinder $R_{\rm LC}$. Using particle-in-cell simulations, we quantify the pulsar spindown for a range of compressions, $R_{\rm m}/R_{\rm LC} = 1/3$–1, and inclination angles, $\chi = 0°\ldots90°$, between magnetic and rotation axes. Our strongly confined models ($R_{\rm m}/R_{\rm LC} = 1/3$) show two distinct limits. For $\chi = 0°$, the spindown of a compressed pulsar magnetosphere is enhanced by approximately a factor of three compared to an isolated pulsar due to the increased number of open magnetic field lines. Conversely, for $\chi = 90°$, the compressed pulsar spins down at less than 40% of the rate of an isolated reference pulsar due to the mismatch between the pulsar wind stripe wavelength and the waveguide size. We apply our analysis to the 2.77 s oblique rotator ($\chi = 60°$) in the double-pulsar system PSR J0737-3039. With the numerically derived spindown estimate, we constrain its surface magnetic field to $B_* \approx (7.3 \pm 0.2) \times 10^{11}$ G. We discuss the time modulation of its period derivative, the effects of compression on its braking index, and implications for the radio eclipse in PSR J0737-3039.

Unified Astronomy Thesaurus concepts: Stellar magnetic fields (1610); Stellar bow shocks (1586); Binary pulsars (153); Pulsars (1306); Plasma astrophysics (1261)

1. Introduction

Pulsars are strongly magnetized rotating neutron stars (NSs) first discovered as multiwavelength pulsating sources in Hewish et al. (1968). The structure of their magnetosphere has been extensively studied in the last 50 years using both analytic methods (e.g., Goldreich & Julian 1969; Ostriker & Gunn 1969; Michel 1973; Scharlemann & Wagoner 1973; Contopoulos et al. 1999; Contopoulos 2005; Gruzinov 2005), as well as simulations (e.g., Spitkovsky 2006; Timokhin 2006; Chen & Beloborodov 2014; Philippov & Spitkovsky 2014, 2018; Ruiz et al. 2014; Pétri 2015; Philippov et al. 2015; Cerutti et al. 2016, 2020; Carrasco et al. 2018; Cruz et al. 2023; Soudais et al. 2024). While the main focus of the community has been drawn to understanding the physics of isolated pulsars, some pulsars are part of binary systems and are not isolated (e.g., Fruchter et al. 1988; Burgay et al. 2003; Crawford et al. 2013). The first discovered double-pulsar system PSR J0737-3039 (Burgay et al. 2003; Lyne et al. 2004) consists of a millisecond pulsar with a period of $P_{\rm A} \sim 22.7$ ms (PSR-A hereafter) and a regular pulsar with a period of $P_{\rm B} \sim 2.77$ s (PSR-B hereafter). The wind from PSR-A likely compresses the magnetosphere of PSR-B to form a bow-shaped magnetopause with the equatorial standoff distance $R_{\rm m}$ of approximately one-third of the light cylinder distance $R_{\rm LC,B} \equiv c/\Omega_{\rm B}$ of PSR-B (Lyutikov 2004; Arons et al. 2005; Lyutikov & Thompson 2005). Here, $\Omega_{\rm B} = 2\pi/P_{\rm B}$ is the angular frequency of PSR-B, and c is the speed of light. Drawing parallels with the nonrelativistic magnetosphere of Earth (e.g., Axford 1962; Russell et al. 2000; Ganguli et al. 2020; Chen et al. 2023), compression may have substantial effects on the magnetospheric geometry and current sheet topology of PSR-B. It likely alters the pulsar's spindown rate, affects the proportion of spindown energy dissipated into particle kinetic energy, and, consequently, affects its multiwavelength emission.

Understanding the multiwavelength emission from pulsars requires theoretical models of their magnetosphere. For an *isolated* pulsar magnetosphere, the charge-separated model proposed by Goldreich & Julian (1969) is a well-established theoretical description of the plasma dynamics: a unipolar induction electric field pulls out plasma from the pulsar to fill the magnetosphere with the so-called Goldreich–Julian (hereafter GJ) charge density $n_{\rm GJ} = \boldsymbol{\Omega} \cdot \boldsymbol{B}/2\pi ec$. Here, $\boldsymbol{\Omega}$ and $\boldsymbol{B}$ are the angular frequency and surface magnetic field of the pulsar (usually considered as a magnetic dipole). In the "plasma-filled" limit of abundant plasma supply, the magnetosphere consists of open field lines extending far away and closed field lines anchored to the star at both ends. The last closed field line touches the light cylinder at the equator. An equatorial current sheet forms beyond $R_{\rm LC}$ due to the reconnection of open magnetic field lines. The energy loss rate (or the "spindown" rate) of a pulsar can be calculated as the surface integral of the Poynting flux, which scales as (Spitkovsky 2006)

$$L_{\rm iso}(\chi) = \frac{\mu^2\Omega^4}{c^3}(1 + \sin^2\chi). \quad (1)$$

Here, μ and χ stand for the dipole magnetic moment and the inclination angle between the rotation and magnetic axes of the

star. The energy dissipated into particle kinetic energy through the equatorial current sheet is approximately 10%–20% of $L_{\rm iso}(0^\circ)$ for aligned pulsars ($\chi = 0^\circ$). Dissipation decreases for larger inclination angles (e.g., Cerutti et al. 2020; Hakobyan et al. 2023). Efficient dissipation in the magnetospheric current sheet is a promising source for the high-energy (X-ray, γ-ray) emission from pulsars (e.g., Cerutti et al. 2016). In this paper, we evaluate how compression by an external wind changes the pulsar spindown and the magnetospheric dissipation. To analyze the effects of magnetospheric compression on current sheet dynamics, it is essential to capture plasma kinetic physics. We use particle-in-cell (PIC) simulations to obtain first-principle predictions of the spindown power for pulsar magnetospheres that are compressed by a companion wind and evaluate the energy budget for particle acceleration and high-energy emission in confined pulsar magnetospheres.

This paper is organized as follows. We describe our computational method in Section 2. Section 2.1 outlines the numerical setup for a wind-enclosed pulsar magnetosphere, and Section 2.2 discusses the shape of the magnetopause enclosure. The results are presented in Section 3 for an aligned pulsar (Section 3.1) and for oblique systems (Section 3.2). In Section 4, we discuss the implications of our findings for the double-pulsar system J0737-3039 as well as limitations and future work (Section 4.2). Finally, Section 5 summarizes our findings. The Appendix comments on the Kelvin–Helmholtz instability at the magnetopause.

2. Methods

We simulate a pulsar magnetosphere confined by a companion wind with the relativistic PIC code TRISTAN-MP (Spitkovsky 2005). In the following, we outline the numerical setup, including the initialization of the pulsar magnetosphere (Section 2.1), and our approach to model the magnetopause enclosure (Section 2.2).

2.1. Setup

We use a 3D Cartesian ($\hat{\boldsymbol{x}}$, $\hat{\boldsymbol{y}}$, $\hat{\boldsymbol{z}}$) mesh with the extent $x \in (-2R_{\rm LC}, R_{\rm LC})$ and $y, z \in (-R_{\rm LC}, R_{\rm LC})$. All simulations performed in this study are evolved for a duration of six rotational periods P. We model the pulsar magnetosphere with inclination χ as a dipole magnetic field $\boldsymbol{B} = (3\boldsymbol{r}(\boldsymbol{\mu}\cdot\boldsymbol{r}) - \boldsymbol{\mu})/r^3$, where $\boldsymbol{r}$ stands for the radial coordinate. Here, the magnetic moment $\boldsymbol{\mu}(t) = \mu(\sin\chi\cos(\Omega t), \sin\chi\sin(\Omega t), \cos\chi)$ is driven by currents in three orthogonal current rings located at the center of the star, where the normals of the rings align with coordinate axes. The NS radius R_* is typically resolved with 50 cells (though high resolution simulations use 100 cells per R_*), and the radius of each current ring is $R_{\rm ring} = 8$ cells with thickness $\Delta_{\rm ring} = 3$ cells ($R_* \gg R_{\rm ring} \gg \Delta_{\rm ring}$). We treat the NS as a perfect conductor, meaning that electric fields inside the star are set to the corotation field $\boldsymbol{E}_{\rm cor} = -(\boldsymbol{\Omega}\times\boldsymbol{r})\times\boldsymbol{B}/c$ at every time step. A smoothing kernel that mitigates Cartesian stair stepping at the spherical NS surface is applied to the electric field boundary condition. The kernel has a hyperbolic tangent profile along the radial direction and a transition width of one cell.

We start our simulations with an NS rotating with $\Omega = c/(6R_*)$ (i.e., nominally $R_{\rm LC} = 6R_*$) and no magnetic fields. We gradually increase the magnetic moment to μ by increasing the current in the rings and allow the magnetosphere to fully establish during an initialization time $t_{\rm ini} \sim 3R_{\rm LC}/c$, or one light-crossing time of the active domain. To mimic a pair cascade in the polar cap, plasma is injected in a thin shell resolved with 10 cells near the NS surface at an injection rate of $n/n_{\rm GJ,*} = 1/3$ and an initial kick with the Lorentz factor of $\gamma_{\rm ini} = 1.33$ along the local magnetic field lines. Here, $n_{\rm GJ,*} \equiv \Omega B_*/2\pi ec$ is the polar GJ density at the NS surface. Inside of the star, we change the velocity of plasma particles such that they fall radially onto the star; particles within $r < 0.4\,R_*$ are removed to prevent charge piling up inside the NS. Outside of the current sheet, we mimic strong synchrotron cooling with an infinitely short cooling timescale by manually damping the momentum perpendicular to the local magnetic field in the $\boldsymbol{E}\times\boldsymbol{B}$ frame of hot and highly magnetized particles (e.g., Hu & Beloborodov 2022).

2.2. Shape of the Magnetopause

To evaluate the geometry of the magnetospheric confinement, we first analyze the interaction between an aligned pulsar ($\chi = 0^\circ$) and a companion wind that forms a magnetopause well within the pulsar's light cylinder upon collision. To model a companion wind, we inject a magnetized plasma flow at the right boundary of our simulation box, propagating along the $-\hat{\boldsymbol{x}}$ direction with a wind Lorentz factor $\gamma_{\rm w} = 50$ and magnetization $\sigma_{\rm w} \equiv B^2/4\pi nm_e c^2 = 0.1$. The wind parameters considered here correspond to those associated with PSR-A (Arons et al. 2005). We prescribe the wind magnetic field along the $+\hat{z}$ axis, parallel to the pulsar magnetic field at the (expected) equatorial collision site to avoid magnetic reconnection.

As shown by the map of pair plasma density in Figure 1, a bow shock structure self-consistently forms. The bow shock (black dashed line) separates the unshocked and shocked wind; the pulsar magnetosphere and the shocked companion wind are separated by the magnetopause (white solid line). Regardless of the pulsar's rotation period, we expect the shape of the magnetopause to be solely dictated by the pressure balance between the pulsar magnetosphere and the companion wind. This balance defines the wind standoff distance $R_{\rm m}$—the equatorial position of the magnetopause—and the opening that delineates the confinement of the wind. Similar to the shape of the Earth's magnetopause from interaction with the solar wind, the pulsar magnetopause in our simulations can be matched with a semiparabolic shape (Shue et al. 1997):

$$\xi_{\rm m} = R_{\rm m}\left(\frac{2}{1+\cos\psi}\right)^{\alpha}, \tag{2}$$

where $\alpha = 0.6$ (see the fitted white solid curve in Figure 1). $\xi_{\rm m}$ is the radial distance at an angle ψ between the NS-wind normal plane (i.e., the equatorial plane here) and the direction of $\xi_{\rm m}$. The magnetopause confines plasma and magnetic field lines emerging from the pulsar (see the inset of Figure 1). Thus, the enclosure acts similarly to a perfect conductor, especially for aligned systems. This work focuses on the effects of compression on the dynamics *well within* the pulsar magnetosphere. For the remainder of this paper, we therefore use a simplified setup that mimics the wind enclosure by a perfectly conducting surface with a paraboloidal shape as prescribed in

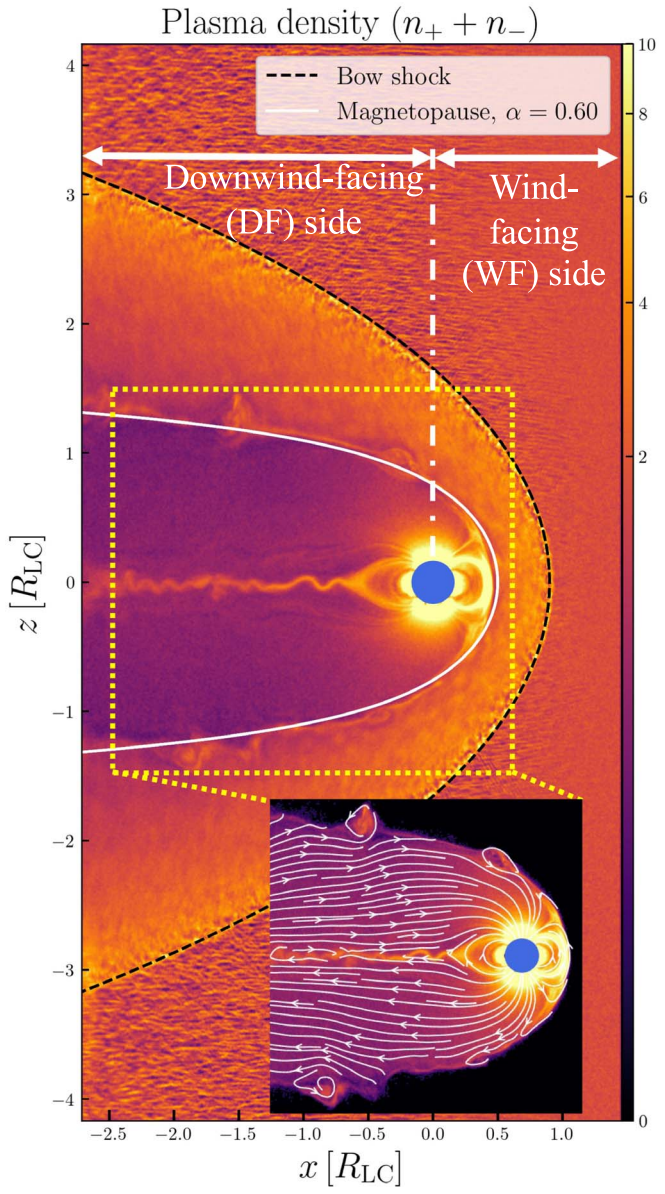

Figure 1. Slice of the 3D pulsar magnetosphere ($y = 0$ plane) with $R_{\rm LC}/R_* = 6$, confined by a companion wind with standoff distance $R_{\rm m}/R_{\rm LC} = 1/2$. We display the total plasma density in the main panel; the inset only includes plasma from the pulsar magnetosphere and magnetic field lines anchored to the pulsar. The bow shock and magnetopause are marked by a black dashed line and a white solid line, respectively. Equation (2) fits the shape of the magnetopause with $\alpha = 0.6$. We split the pulsar magnetosphere into the "wind-facing" (WF) side directed toward the origin of the companion wind and the "downwind-facing" (DF) side that faces along the flow direction of the wind.

Equation (2). We apply the same smoothing kernel to this curved boundary of the perfectly conducting wind enclosure as at the NS surface (Section 2.1).

3. Results

We simulate pulsar magnetospheres compressed with $R_{\rm m}/R_{\rm LC} \lesssim 1$, where the wind enclosure is modeled by a perfect conductor with the shape given by Equation (2). As representative cases, we show the results for aligned rotators ($\chi = 0°$) with varying standoff distances $R_{\rm m}$ in Section 3.1, and different oblique rotators ($\chi \neq 0°$) confined with $R_{\rm m}/R_{\rm LC} = 1/3$ in Section 3.2.

3.1. Aligned Rotators

For aligned rotators, plasma dynamics are driven by the unipolar inductor electric fields. Figure 2 shows a snapshot of the magnetospheric structure of a pulsar confined with $R_{\rm m}/R_{\rm LC} = 1/3$ after three rotation periods. Panel (b) indicates that the plasma is well magnetized with $\sigma \gtrsim 100$ inside the light cylinder (white dotted line). Despite the compression, the characteristic configuration of open and closed field lines typical of isolated pulsar magnetospheres is preserved, as shown in panel (c). The wind-facing (WF) side of the magnetosphere has a compressed closed zone of reduced size compared to the downwind-facing (DF) side; the open field lines follow the shape of the wind enclosure and extend to the left boundary of the domain. An equatorial current sheet forms between open field lines of opposite polarity on the DF side (panels (d) and (e)). Panel (f) indicates that most of the Poynting flux is carried on the open magnetic field lines.

Due to the wind compression, the quasi-steady field structure shown in Figure 2 is nonaxisymmetric about the pulsar's rotational axis. For $R_{\rm m}/R_{\rm LC} < 1$, the closed zone on the WF side is compressed to approximately fit the enclosure size $R_{\rm m}$ without forming an equatorial current sheet. Open field lines emerging on the WF side extend along the wind enclosure in layers 1 and 4 (Figure 2(c)). They carry out-of-plane magnetic fields with opposite polarity but do not reconnect in the regime we explored. Open field lines emerging from the DF side (layers 2 and 3) are enveloped by those originating on the WF side (layers 1 and 4). They reconnect and form an equatorial current sheet from the magnetic Y-point, located inside the light cylinder at $R_{\rm Y} \approx 0.57 R_{\rm LC}$. The Y-point displacement leads to more open magnetic flux than for isolated pulsars (where commonly $R_{\rm Y} \approx R_{\rm LC}$). Consequently, the spindown rate is enhanced compared to Equation (1). In the presented PIC simulation, we measure reconnection rates of $\beta_{\rm rec} \approx 0.3...0.4$ on the DF side (Figure 2(d)), twice larger than the typical value $\beta_{\rm rec} \approx 0.1...0.2$ observed in simulations of isolated pulsars (e.g., Werner et al. 2018; Hakobyan et al. 2023). This dissipation can be seen as the bright region in Figure 2(e). During one period, an open field line initially in layer 2 (or 3) on the DF side will be in layer 1 (or 4) when rotating to the WF side. A closed field line that extends beyond the equatorial radius $r_c > R_{\rm m}$ on the DF side experiences compression at the enclosure boundary when rotating to the WF side. In our simulations, we find that this compression results in a change of the toroidal velocity of these compressed field lines, empirically $\partial v_\varphi/\partial t \sim \Omega^2 (R_{\rm m} - R_{\rm Y})$ for $R_{\rm m} < R_{\rm Y}$. The compressive drag induces poloidal currents and a toroidal magnetic field at the outer edge of the closed zone $r \approx R_{\rm m}$ (Figure 2(c)).

To quantify the relation between the pulsar spindown rate for varying magnetospheric compression ($R_{\rm m}/R_{\rm LC} = 1/3,\ 1/2,\ 2/3,\ 5/6,\ 1$), we analyze radial profiles of the Poynting flux integrated at concentric shells with radius r:

$$L_r(r) \equiv \frac{c}{4\pi} \oiint_r (\boldsymbol{E} \times \boldsymbol{B}) d\boldsymbol{S}. \quad (3)$$

Figure 3 shows the radial profiles of the Poynting flux normalized to $L_{\rm iso}(\chi = 0°)$. We measure the spindown luminosity as the nondecaying "plateau" $L_{r,\rm pla}$ within $r \lesssim R_{\rm m}$ (see the black rectangular box in Figure 3). In all cases, the outgoing luminosity experiences a strong decay beyond $r \sim R_{\rm m}$. This energy loss accounts for 40%–60% of the spindown luminosity. Similar to an isolated pulsar, energy dissipation in a

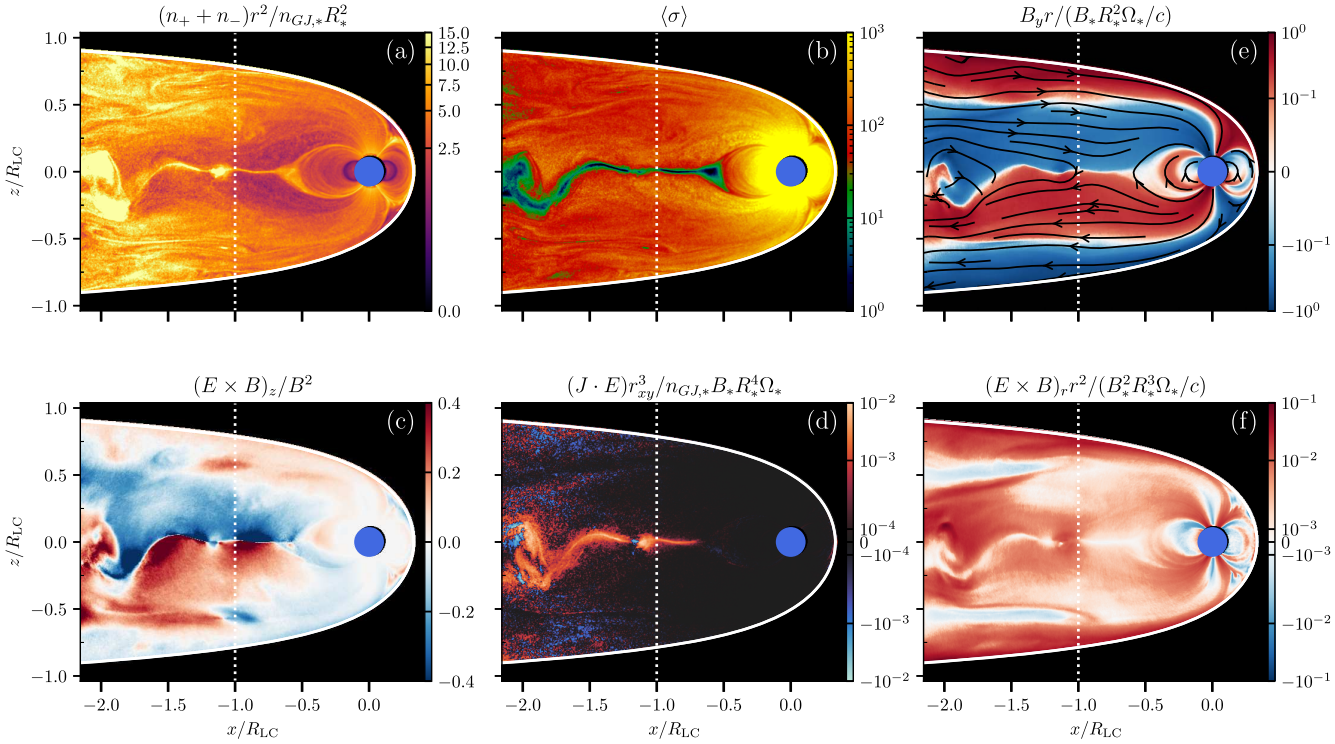

Figure 2. Magnetospheric structure of the aligned pulsar magnetosphere with confinement $R_{\rm m}/R_{\rm LC} = 1/3$ (slice in the x–z plane of a 3D simulation; rotation axis is parallel to $\hat{z}$). We show (a) the plasma density $n \equiv n_+ + n_-$ normalized by the polar GJ density at the surface $n_{\rm GJ,*}$, (b) the plasma magnetization $\sigma \equiv B^2/4\pi n m_e c^2$, (c) the out-of-plane magnetic field B_y, (d) the reconnection rate $(\boldsymbol{E}\times\boldsymbol{B})_z/B^2$, (e) the volume dissipation rate $\boldsymbol{J}\cdot\boldsymbol{E}$, and (f) the radial Poynting flux $c\,(\boldsymbol{E}\times\boldsymbol{B})_r/4\pi$. The snapshot is taken at $t = 3.09P$. The white solid curves show the boundary of a perfect conductor with the shape prescribed by Equation (2). An animated version of this figure is available as supplementary material (https://youtu.be/Oobs6lbhH48).

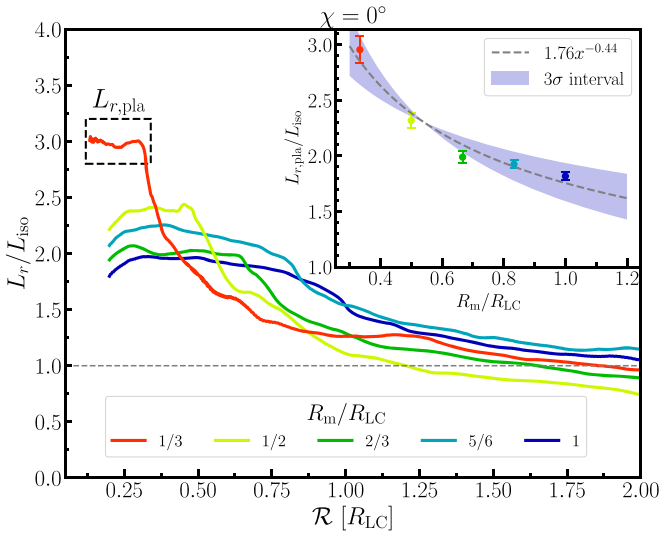

Figure 3. Radial dependence of the surface-integrated Poynting flux in aligned pulsars confined with $R_{\rm m}/R_{\rm LC} = 1/3,\ 1/2,\ 2/3,\ 5/6,\ 1$. The inset shows the plateau value $L_{r,\rm pla}$ as a function of $R_{\rm m}/R_{\rm LC}$. Time variability is shown as error bars, and the gray dashed line denotes the fitted function with 3σ confidence interval (blue shaded region).

confined magnetosphere mainly happens at the current sheet on the DF side, where magnetic reconnection occurs (Figure 2(c)). However, since the net energy loss rate is enhanced compared to the isolated reference pulsar (Equation (1)) and the reconnection rate is higher on the DF side, the current sheet in confined magnetospheres converts electromagnetic energy into particle kinetic energy more efficiently. This contrasts with typical isolated pulsar magnetospheres (see, e.g., Cerutti et al. 2016; Hakobyan et al. 2023), where dissipation occurs at a rate of approximately 10%–20% of $L_{\rm iso}(0°)$ beyond the light cylinder. The kinetic energy attainable by particles in the current sheet can be estimated by the plasma magnetization at the magnetic Y-point as $\langle\gamma\rangle_{\rm max} \sim \sigma_{\rm Y} \equiv (B^2/4\pi(n_+ + n_-)m_e c^2)_{\rm Y}$, where our simulations show $\sigma_{\rm Y} \approx 300$ for $R_{\rm m}/R_{\rm LC} = 1/3$.

By fitting the net energy loss rate $L_{r,\rm pla}$ for different $R_{\rm m}/R_{\rm LC}$, we find the spindown luminosity $L_{r,\rm pla}$ to be *enhanced* by a factor of

$$\frac{L_{r,\rm pla}}{L_{\rm iso}(0°)} \sim a\left(\frac{R_{\rm m}}{R_{\rm LC}}\right)^{\varepsilon}, \tag{4}$$

where the best-fit parameters are found to be $a = 1.76$ and $\varepsilon = -0.44$, as shown in Figure 3. This enhancement is mainly due to the larger open magnetic flux when the magnetic Y-point $R_{\rm Y}$ is inside the light cylinder. By measuring $R_{\rm Y}$ for different $R_{\rm m}/R_{\rm LC}$, we find the enhancement to scale with

$$\frac{L_{r,\rm pla}}{L_{\rm iso}(0°)} \sim \left(\frac{R_{\rm Y}}{R_{\rm LC}}\right)^{-2}, \tag{5}$$

which is broadly consistent with the scaling given by Timokhin (2006). Here, $R_{\rm Y}$ varies with the magnetospheric confinement parameter; hence, the power law index in Equation (5) is different from ε in Equation (4). Finding ε enables us to discuss the braking index $n \equiv \Omega\,\ddot{\Omega}/\dot{\Omega}^2 = 3 + \varepsilon$ of a confined pulsar magnetosphere. Time variability of the spindown induces uncertainties to the fit, which we denote as error bars in the inset panel of Figure 3. However, this variability is generally

small and lies mostly within the 3σ confidence interval of the regression. We thereby estimate the braking index for aligned pulsars confined by a companion wind as $n \approx 2.56$ for $R_m/R_{LC} \lesssim 1$. We note that this braking index is expected to change when R_m/R_{LC} increases and surpasses unity. When the strength of the companion wind decays, Equation (4) will gradually increase until reaching a value of 3, the anticipated index for an isolated pulsar magnetosphere.

3.2. Oblique Rotators

In this section, we present the results for oblique rotators ($\chi \neq 0°$) confined with $R_m/R_{LC} = 1/3$. As a reference, we analyze an orthogonal rotator in a vacuum to discuss how the electromagnetic field structure and the resulting spindown differ in a plasma-filled magnetosphere. We will identify magnetospheric dynamics of oblique rotators as an interplay of the characteristic features of aligned and orthogonal rotators.

Vacuum orthogonal rotators have time-varying magnetic fields that induce electromagnetic waves that carry away energy with spindown luminosity,

$$L_{vac}(\chi) = \frac{2}{3}\frac{\mu^2\Omega^4}{c^3}\sin^2\chi, \tag{6}$$

and a wavelength of $2\pi R_{LC}$. In a waveguide with a size smaller than half of this wavelength—the wind enclosure in our context—electromagnetic waves cannot propagate (J. Epstein et al. 2024, in preparation). This is the so-called waveguide cutoff effect (Jackson 1975). Figure 4(i) shows the field structure of a vacuum orthogonal rotator confined by a wind enclosure at $R_m/R_{LC} = 1/3$. By analyzing the poloidal electric field (panel (a)), the toroidal magnetic field (panel (b)), and the radial Poynting flux (panel (c)), we infer two main aspects of the dynamics. First, similar to isolated vacuum orthogonal rotators, all field lines are closed and do not extend from the surface to infinity. Second, both E_θ and B_φ decay faster than $1/r$, resulting in an attenuation of the Poynting flux at a larger distance from the pulsar. This can also be seen by analyzing the radial dependence of the luminosity enhancement $L_r/L_{vac}(90°)$ at different time steps (thin black sequence in Figure 5(a)). The time-averaged luminosity $\overline{L_r}$ vanishes (thick black curve in Figure 5(a)), consistent with the zero energy loss rate, as expected from the waveguide cutoff effect. In other words, this rotator does not spin down. The term "cutoff" does not denote the complete absence of electromagnetic fields in the magnetosphere. Instead, it means that waves become evanescent: electromagnetic oscillations cannot propagate, resulting in the termination of electromagnetic outflow from a confined vacuum orthogonal rotator. This feature can be seen from the time evolution of the resulting integrated Poynting flux (thin black curves in Figure 5(a)).

Plasma-filled orthogonal rotators with $R_m/R_{LC} = 1/3$ have field structures as shown in Figure 4(ii). We display the equatorial plane at the same moment in physical time as the vacuum reference in Figure 4(i) for a direct comparison. Notably, the plasma density (Figure 4(ii)(d)) and the current component J_z (Figure 4(ii)(f)) show a plasma blob decoupling from the magnetosphere, accompanied by a current sheet. This blob bends the magnetic field lines (Figure 4(ii)(b)) and carries Poynting flux from the pulsar (Figure 4(ii)c). The volume dissipation associated with the current sheet is shown in Figure 4(ii)(e).

Figures 5(b)–(d) display the radial dependence of the luminosity enhancement $L_r/L_{iso}(\chi)$ for plasma-filled rotators with varying inclination χ and fixed magnetospheric confinement, $R_m/R_{LC} = 1/3$. Thin lines denote the local enhancement for different time steps, while thick lines are time averages $\overline{L_r}/L_{iso}$. Analyzing radial luminosity distributions allows us to outline key characteristics of confined oblique pulsar magnetospheres. In contrast to the vacuum reference (Figure 5(a)), plasma-filled orthogonal rotators have an outward electromagnetic energy flux with peak luminosity locations varying with time (Figure 5(d), thin lines). For $\chi = 90°$, we measure[5] a nonzero spindown rate of approximately $0.4\,L_{iso}(90°)$ that decays with radius (thick line). This spindown rate is still suppressed compared to the rate of the corresponding isolated reference pulsar, mainly because the cavity size is well below the waveguide cutoff limit. The peak dynamics and decay are likely driven by the motion of the plasma blob that carries energy and dissipates it within the current sheet. For $\chi = 60°$ (Figure 5(c)), we find the time-averaged luminosity nearly stable inside the wind standoff distance. With time variability (thin lines) similar to the orthogonal rotator, the extended plateau $\overline{L_{r,pla}}$ for $\chi = 60°$ is closer to the aligned rotator profile ($\chi = 0°$, thick line in Figure 5(b)). Intermediate inclination angles $0° < \chi < 90°$ thus display an interplay of aligned rotator and orthogonal rotator features. The net energy loss of the $\chi = 60°$ rotator is approximately $1.06\,L_{iso}(60°)$. This spindown energy is carried by Poynting flux close to the NS ($r \lesssim R_m$), and approximately 50% of it dissipates into particle kinetic energy up to $r \approx R_{LC}$. In summary, we outline two main takeaways for confined pulsar magnetospheres with inclination. First, the spindown rate is *enhanced* by a factor of 3 for the aligned rotator (Figure 5(b)), while it is *suppressed* by a factor of approximately 0.4 for the orthogonal rotator (Figure 5(d)). Second, the time variability of the spindown rate is small for an aligned rotator (Figures 5(b) and 3), but can be significant for orthogonal rotators (Figures 5(c) and (d)).

In Figure 6, we show a representative snapshot of the field geometry and current sheet topology for a $\chi = 60°$ rotator confined with $R_m/R_{LC} = 1/3$. At $t = 3\,P$, the chosen visualization plane (x–z) corresponds to the plane spanned by the magnetic moment $\boldsymbol{\mu}$ and the angular frequency $\boldsymbol{\Omega}$. Similar to the aligned rotator (Figure 2), the magnetosphere is confined on the WF side and free to expand on the DF side. The plasma is still strongly magnetized, with $\sigma \gtrsim 100$ (Figure 6(b)). However, a nonzero inclination angle between $\boldsymbol{\mu}$ and $\boldsymbol{\Omega}$ causes field lines to stretch and extend to infinity at different rotational phases. This "wobbling" results in a time variability of the polar cap size throughout the pulsar rotation period. As a geometric effect, this phenomenon may lead to variations in the shape of the pulse profile observed at different rotational phases, depending on the specific locations of emission zones. Another consequence of the tilted magnetic axis is that the current sheets no longer primarily form in the equatorial plane, as shown in Figures 4(d) and 6(a). For instance, Figure 6(c) indicates that a significant confluence of magnetic field lines with opposite polarity occurs primarily in the upper current

[5] In practice, we use Poynting's theorem to estimate the spindown rate of oblique systems. By adding the time-averaged outgoing luminosity L_r and the time-averaged volume dissipation rate $\boldsymbol{J}\cdot\boldsymbol{E}$, we obtain an average net energy loss rate that can be used as a robust estimate of the spindown power.

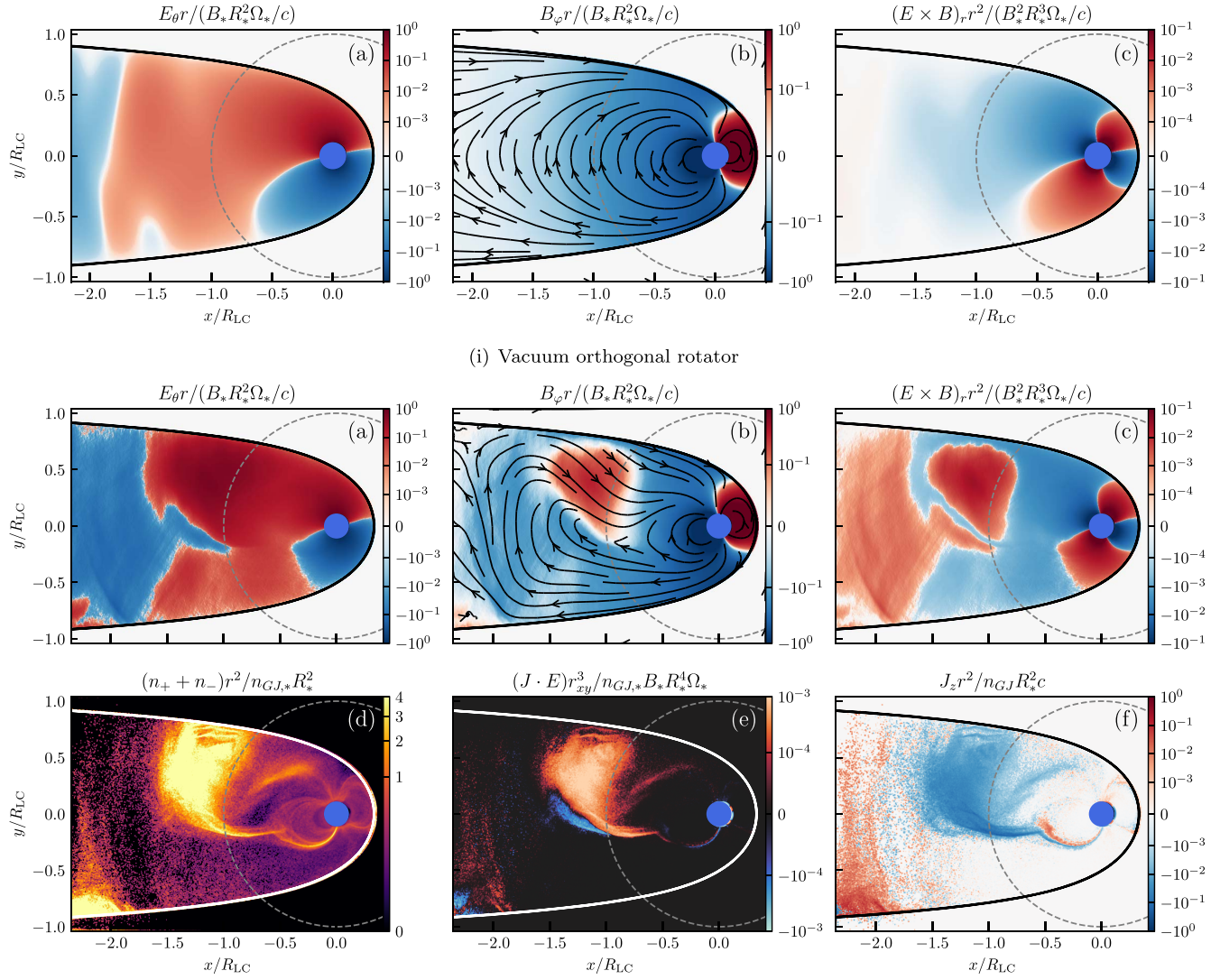

Figure 4. Magnetospheric structure for confined orthogonal rotators with $R_m/R_{LC} = 1/3$ (i) in a vacuum (top three panels) and (ii) with plasma (bottom six panels). (a) poloidal electric field E_θ; (b) toroidal magnetic field B_φ; (c) radial Poynting flux $c\ (\boldsymbol{E} \times \boldsymbol{B})_r/4\pi$; (d) plasma density normalized by polar cap GJ density at the surface $n_{GJ,*}$; (e) volume dissipation rate $\boldsymbol{J} \cdot \boldsymbol{E}$; and (f) z-component of the conduction current J_z in the x–y plane (i.e., equatorial plane). The snapshot is taken at $t = 3.28\ P$. The solid curves show the boundary of a perfect conductor with the shape prescribed by Equation (2). Animated versions of panels (i) and (ii) are available as supplementary material (panel (i): https://youtu.be/EvuU4Yk3uWw; panel (ii): https://youtu.be/UQhHwtU7q6k).

sheet. There, the reconnection rate shows flows into sheet-like structures (Figure 6(c)) and dissipation is the strongest (Figures 6(d) and (e)). The Poynting flux is still predominantly carried on the open field lines, as shown in Figure 6(f).

4. Discussion

Guided by our simulation results, we first discuss implications for the double-pulsar system PSR J0737-3039 in Section 4.1, and then address some caveats of our numerical simulations and outline future work in Section 4.2.

4.1. Implications for PSR J0737-3039

As introduced in Section 1, the double-pulsar system PSR J0737-3039 consists of one millisecond pulsar PSR-A with $P_A \approx 22.7$ ms, inclined with $\chi_A \approx 4^\circ \pm 3^\circ$ (Burgay et al. 2003; Demorest et al. 2004), and one ordinary pulsar PSR-B with $P_B \approx 2.77$ s, inclined with $\chi_B \approx 60^\circ...70^\circ$ (Lyne et al. 2004; Breton et al. 2008; Perera et al. 2014). The orbital plane is almost edge-on (inclination angle $\approx 88^\circ.7$; see, e.g., Kramer et al. 2006), and the orbital period is 2.48 hr. This system has many interesting emission properties. The flux and pulse profile structure of PSR-B showed strong variations with orbital phase and underwent a radio disappearance since 2008 as its beam precessed out of our line of sight. On the other hand, PSR-A has a stable pulse profile with two components and a 30 s eclipse when it passes behind PSR-B (Lyne et al. 2004; Lyutikov & Thompson 2005). As a millisecond pulsar with a larger spindown rate $\dot{E}_A \approx 5.8 \times 10^{33}$ erg s^{-1} (compared to PSR-B with $\dot{E}_B \approx 1.6 \times 10^{30}$ erg s^{-1}), PSR-A is believed to emit a highly relativistic and persistent pulsar wind that interacts with the magnetosphere of PSR-B and produces a magnetopause at $R_m/R_{LC,B} \approx 1/3$ (e.g., Lyutikov 2004; Arons et al. 2005).

Directly applying our findings of the spindown power of an oblique pulsar ($\chi = 60^\circ$) confined by a wind enclosure

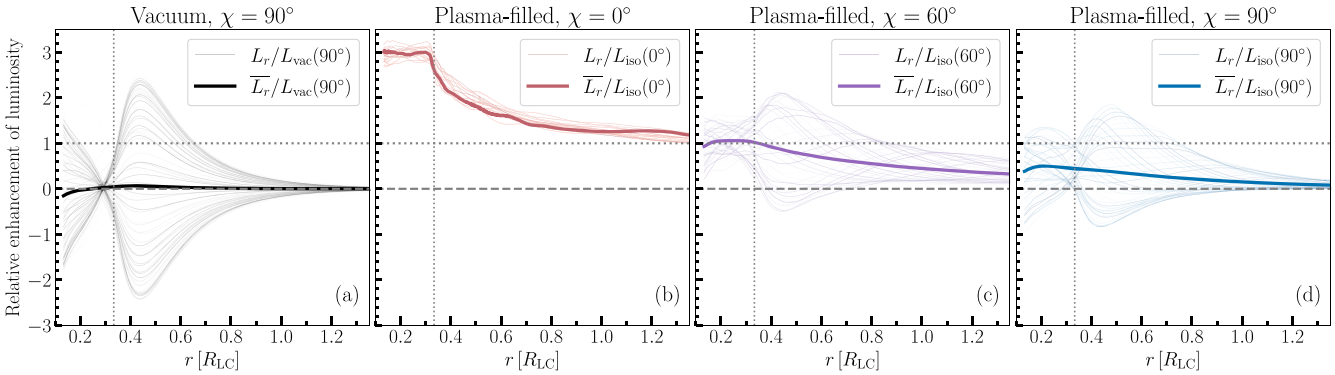

Figure 5. Relative enhancement of Poynting luminosity for rotators with magnetospheric confinement parameter $R_{\rm m}/R_{\rm LC} = 1/3$. Thin lines show instantaneous radial profiles of Poynting flux, measured using Equation (3), with different curves denoting time evolution over a rotation period. The time-averaged profiles, $\overline{L_r}$, are shown as thick lines. We analyze compressed magnetospheres with different plasma supply and inclinations: (a) vacuum orthogonal rotator, with the luminosity on the *y*-axis normalized by the isolated vacuum spindown luminosity (Equation (6)); (b) plasma-filled aligned rotator (red curve in Figure 3); (c) plasma-filled orthogonal rotator; and (d) plasma-filled 60° rotator. The luminosity profiles of all plasma-filled rotators (panels (b), (c), and (d)) are normalized by the corresponding isolated spindown rate given by Equation (1). Horizontal dashed lines denote zero energy loss, horizontal dotted lines denote the spindown of an isolated pulsar (i.e., no luminosity enhancement), and vertical dotted lines indicate the standoff distance $R_{\rm m}$.

(Figure 5(c)), we expect PSR-B to spin down with

$$\dot{E} \approx (1.02 \pm 0.04)\, L_{\rm iso}(60°). \tag{7}$$

Here, the error bar reflects the uncertainty of measurement due to the radial dependence of integrated luminosity inside the standoff radius $R_{\rm m}$ in Figure 5(c). By equating Equation (7) to the spindown rate of PSR-B, we find

$$L_{\rm sd} \equiv -\frac{dE_{\rm rot}}{dt} = \frac{4\pi^2 I \dot{P}}{P^3}, \tag{8}$$

where $I_{\rm B} = 2M_{\rm B}R_*^2/5$ is the moment of inertia of PSR-B, and the period derivative reads $\dot{P}_{\rm B} \approx 0.88 \times 10^{-15}$ s s^{-1} (Lyne et al. 2004). The surface magnetic field strength of PSR-B can then be estimated as $B_* \approx (7.3 \pm 0.2) \times 10^{11}$ G. Our estimate for the magnetic field is close to that of Arons et al. (2005), as the spindown power for the $\chi = 60°$ rotator in our model coincidentally matches that of an isolated force-free pulsar. This estimate barely changes while considering $\chi \sim 60°...75°$, where the upper limit here is the best-fit parameter obtained by Lyutikov & Thompson (2005). In fact, even if we did not have good observational constraints on χ, our simulations indicate that the maximum and minimum expected spindown luminosities are approximately $\dot{E}_{\rm max} \approx 3\, L_{\rm iso}(0°)$ and $\dot{E}_{\rm min} \approx 0.4\, L_{\rm iso}(90°)$, respectively. This range allows us to constrain PSR-B's surface magnetic field to be in the fairly narrow range, $B_* \approx (0.5...1.0) \times 10^{12}$ G.

The spindown power (Equation (7)) is affected by the magnetospheric compression parameter $R_{\rm m}/R_{\rm LC}$, which is expected to vary over the orbital phase due to orbital eccentricity. This should induce a time modulation of the observed period derivative, $\dot{P}_{\rm B}$, of PSR-B. To constrain the magnitude of this effect, we assume PSR-B to be an aligned pulsar, where the radial luminosity profiles are time-independent, and the dependence of spindown luminosity on $R_{\rm m}/R_{\rm LC,B}$ is given by Equation (4). Combining Equations (1), (5), and (8), we obtain

$$\dot{P}_{\rm B} P_B^{0.56} \propto R_{\rm m}^{-0.44}. \tag{9}$$

Here, $R_{\rm m}$ is determined by the pressure balance between the wind from PSR-A and the magnetic field of PSR-B. Given that the distance between the two pulsars, $D_{\rm AB}$, varies with the orbital phase for eccentricity $e \sim 0.088$, the orbital modulation of $\dot{P}_B$ can be estimated as

$$\frac{|\Delta \dot{P}_{\rm B}|}{\dot{P}_{\rm B}} \sim 0.44 \frac{|\Delta R_{\rm m}|}{R_{\rm m}} \sim 0.22 \frac{|\Delta D_{\rm AB}|}{D_{\rm AB}} \sim 0.44e \approx 4\% \tag{10}$$

to the leading order, where we use $R_{\rm m} \propto D_{\rm AB}^{1/2}$ (e.g., Lyutikov 2004). This is within the error bar of the measurements by Lyne et al. (2004), which is around 15%.

We estimate the braking index of aligned rotators with magnetospheric confinement parameters $R_{\rm m}/R_{\rm LC} < 1$ as $n = 2.56$ in Equation (9) and Section 2.2. This value is below the anticipated value of $n = 3$ for isolated (dipolar) pulsar magnetospheres, likely due to the Y-point being inside the light cylinder. For oblique rotators with $\chi \sim 60°...70°$, n should be closer to 3, since the enhancement of spindown caused by the Y-point located inside the light cylinder is partially compensated by the waveguide cutoff effects when the magnetospheric confinement parameter is $R_{\rm m}/R_{\rm LC} \approx 1/3$. As n increases and approaches 3, the modulation derived in Equation (10) will decrease. Therefore, the time modulation estimated above is likely at its maximum for $\chi = 0°$. We note also that, while compressed magnetospheres can have braking indices <3, the problem of the deviation of observed braking indices of *isolated* pulsars from the expected dipolar value is still unresolved (e.g., Kaspi & Helfand 2002; Livingstone et al. 2007; Magalhaes et al. 2012). The physics that ultimately reconciles braking indices for isolated pulsars with observations (that likely has to do with the details of the Y-point reconnection) may also impact the braking index of the compressed magnetospheres studied here.

One interesting feature developing in simulations of a tightly confined aligned pulsar magnetosphere is the toroidal twist of the magnetic field at the outer edge of the closed zone (Section 3.1), due to the compression of closed field lines when they rotate from the DF side to the WF side. This twist occurs only in tightly confined cases, with the standoff distance on the WF side being $R_{\rm m} < R_{\rm Y}$ (e.g., our setup with $R_{\rm m}/R_{\rm LC} = 1/3$). A similar magnetospheric twist was proposed in a model for the 30 s radio eclipse (Lyutikov & Thompson 2005). There, the twist launches torsional Alfvén waves responsible for drawing sufficient plasma ($n/n_{\rm GJ} \sim 10^{4...5}$) into the closed zone of PSR-

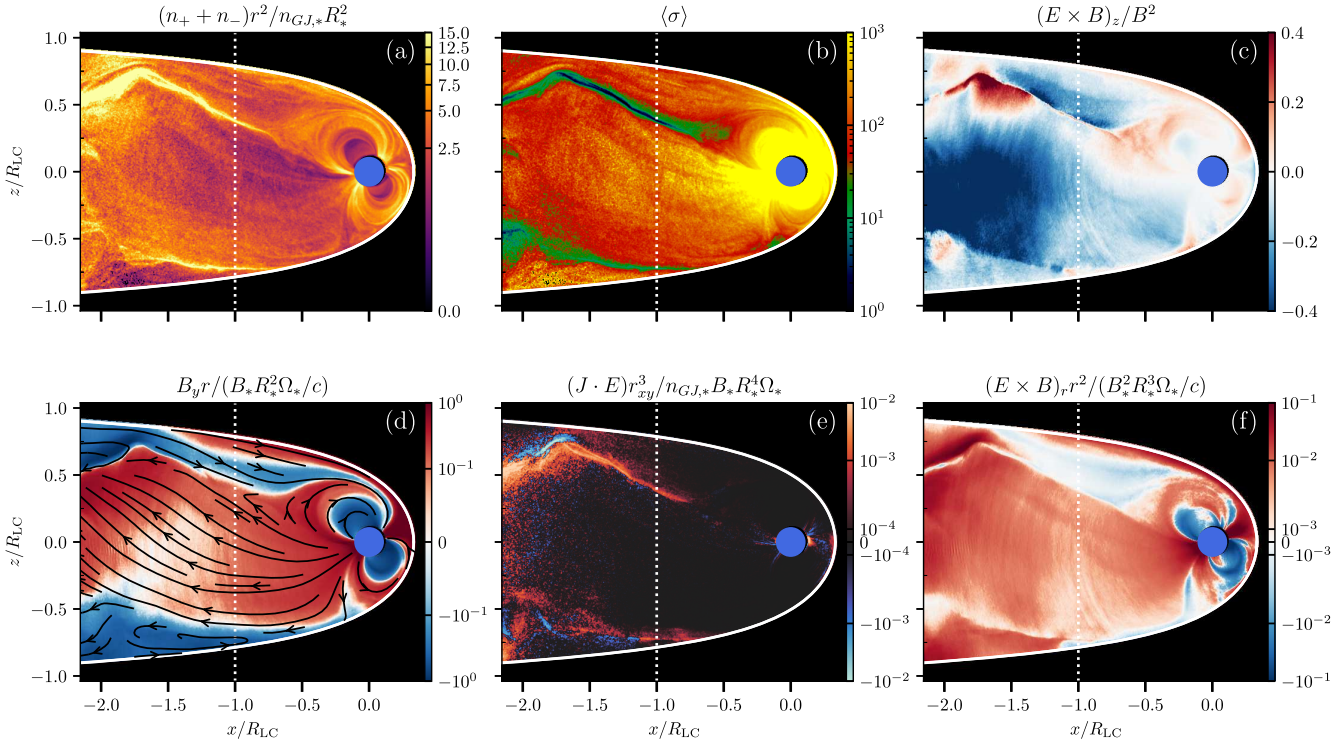

Figure 6. Magnetospheric structure for a confined pulsar magnetosphere with $\chi = 60^\circ$ and $R_{\rm m}/R_{\rm LC} = 1/3$ (x–z plane of a 3D simulation). We show (a) the plasma density normalized by polar cap GJ density at the surface $n_{\rm GJ,*}$, (b) the plasma magnetization $\sigma \equiv B^2/4\pi n m_e e^2$, (c) the reconnection rate $(\boldsymbol{E} \times \boldsymbol{B})_z/B^2$, (d) the out-of-plane magnetic field B_y, (e) the ohmic dissipation rate $\boldsymbol{J} \cdot \boldsymbol{E}$, and (f) the radial Poynting flux $c\ (\boldsymbol{E} \times \boldsymbol{B})_r/4\pi$. The snapshot is taken at $t = 3.00\ P$. The white solid curves show the boundary of a perfect conductor with the shape prescribed by Equation (2). An animated version of this figure is available as supplementary material (https://youtu.be/LD6eCSsPV6I).

B to produce the radio eclipse by achieving a cyclotron absorption optical depth of $\tau_\nu \sim 1$.

4.2. Limitations and Future Work

The shape of the boundary between the magnetosphere and the wind forms self-consistently due to the pressure balance between the magnetic field and the companion wind. As was justified in Section 2.1, we prescribe the magnetopause as a perfect conductor in our simulations. While this treatment is sufficient for studying the dynamics of the confined magnetosphere, it does not allow us to model the plasma mixing between the magnetosphere and the wind. For instance, Kelvin–Helmholtz instability can form at the pulsar magnetopause and mix plasma from the companion wind and the pulsar magnetosphere (Appendix), potentially causing extra dissipation. Plasma loading of the magnetosphere from the wind is crucial for comparing with the double-pulsar eclipse model presented in Lyutikov & Thompson (2005), which requires high plasma multiplicity in the outer regions of the closed zone of PSR-B to explain the eclipse. Also, our model does not account for the morphology of the double-pulsar system, such as relative inclination of the compressed pulsar rotation axis to the orbital plane, which facilitates orbital phase-dependent changes in the enclosure shape. For weaker winds with $R_{\rm m}/R_{\rm LC} \sim 1$, we observe the reemergence of the current sheet on the WF side for an aligned rotator. The current structure develops within the wind standoff distance and extends to the perfect conductor. Incorporating a real companion wind would help us understand how this current sheet affects the shape of the magnetopause. Confined orthogonal rotators exhibit significant variability in their magnetic fields and Poynting fluxes (Section 3.2). The response of the magnetopause shape to this time variability remains unclear.

A key result of Section 3.2 is that orthogonal rotators confined with $R_{\rm m}/R_{\rm LC} = 1/3$ spin down with the rate of approximately $0.4\,L_{\rm iso}(90^\circ)$ for plasma-filled magnetospheres, while they do not experience a net energy loss in a vacuum due to the waveguide cutoff effect. It remains an open question whether the presence of plasma changes the vacuum waveguide cutoff limit or if it introduces the possibility for the electromagnetic energy of the evanescent wave to dissipate via the current sheet.

The structure of tightly confined aligned rotators with $R_{\rm m}/R_{\rm LC} \lesssim 1/3$ deviates from the models described in this paper. The spindown rate of confined aligned rotators scales with the rotation frequency as $L_{r,\rm pla} \propto \Omega^{3.56}$ (Equation (4)). Consequently, when Ω becomes small, the outgoing Poynting flux sharply decreases. The dipole pressure, which decays as r^{-6}, then becomes the dominant force balancing the wind pressure and causes the magnetopause cavity to converge. Without sufficient toroidal magnetic pressure support, the size of the DF magnetopause opening becomes smaller; the magnetopause shape is no longer a parabola but becomes tear shaped. Such dynamics of the magnetopause can backreact on the inner magnetosphere and further suppress the resulting spindown luminosity. We will quantify the effects of this suppression in a future work.

Another aspect overlooked in the perfect conductor approximation of the pulsar-wind boundary is the magnetic reconnection occurring at the magnetopause. This becomes significant in the context of a companion wind from an oblique rotator, where its toroidal magnetic field forms striped patterns

with alternating polarity, separated by current sheets at latitudes lower than the inclination angle χ. As the flow compresses at the shock, the alternating fields annihilate via magnetic reconnection (e.g., Sironi & Spitkovsky 2011; Cortés & Sironi 2022). The field remaining after this "shock-driven reconnection" will reconnect with the magnetospheric field of the pulsar at the magnetopause. Observationally, this will modulate the pressure on the magnetosphere at the rotational frequency of the oblique rotator (e.g., for PSR-A; McLaughlin et al. 2004), and will exert additional torques on the confined pulsar (e.g., Arons et al. 2005). Our future work will quantify this time modulation and will evaluate how particle spectra and pulsar spindown vary due to reconnection events at the magnetopause and the bow shock in PSR J0737-3039.

Finally, our general understanding of plasma dynamics within the magnetosphere of PSR-B remains incomplete. Pair production processes in the magnetospheres of energetic pulsars have been extensively studied (e.g., Timokhin & Harding 2019). However, the maximum amount of pair plasma generated in the polar cap and the fraction that reaches the Y-point for slowly rotating pulsars like PSR-B are not well constrained. A related issue is the expected high-energy emission from PSR-B-like systems. As we have shown in Section 3.2, a $\chi = 60^\circ$ rotator confined with $R_m/R_{LC} = 1/3$ is expected to spin down at a rate of $\sim 1.06\, L_{iso}(60^\circ)$. It dissipates approximately 50% of the outgoing Poynting flux into particle kinetic energy within one light cylinder distance away from the star through magnetic reconnection in the current sheets. These energized particles are expected to produce pulsed emission via synchrotron radiation (e.g., Cerutti et al. 2016; Philippov & Spitkovsky 2018), with the characteristic photon energy determined by the pair production processes in the polar cap and near the Y-point. For slowly rotating pulsars, where the cooling can be weak, the emission processes remain less understood. Self-consistent studies on plasma supply and radiation processes in the magnetosphere of slowly rotating pulsars are required to accurately describe their plasma state.

5. Conclusions

We use PIC simulations to investigate the change of pulsar spindown under significant compression due to its interaction with a companion wind. We find that, depending on the magnetic inclination, χ, this compression can either enhance or suppress the spindown luminosity compared to the net energy loss of an isolated pulsar (Equation (1)). We identify two distinct limits:

1. *Luminosity-enhancing limit:* magnetospheric compression enhances the spindown rate for aligned rotators because the amount of open magnetic flux increases due to compression within the light cylinder (Y-point shifted inwards). Unlike isolated pulsars, the wind-enclosed magnetosphere is nonaxisymmetric. The enclosure guides open field lines along the cavity on the WF side, while a current sheet forms on the DF side. The measured reconnection rate $\beta_{rec} \approx 0.3...0.4$ exceeds the typical value expected from the isolated pulsar: $\beta_{rec} \approx 0.1...0.2$ (e.g., Cerutti et al. 2020; Hakobyan et al. 2023).
2. *Luminosity-suppressing limit*: magnetospheric compression suppresses the spindown rate for orthogonal rotators due to the waveguide cutoff effect. In a vacuum, the spindown ceases completely for strong compression ($R_m/R_{LC} = 1/3$). However, a plasma-filled rotator can spin down by forming intermittent plasma blobs and current sheets. Then, the spindown energy is transported by Poynting flux within the standoff distance. Beyond this region, part of the electromagnetic energy dissipates by energizing particles in current sheets. The remaining Poynting flux is primarily carried by the outflowing plasma blobs.

As the interplay of these two limits, a $\chi = 60^\circ$ rotator confined with $R_m/R_{LC} = 1/3$ spins down at a rate similar to that predicted for isolated pulsars by Equation (1). Approximately 50% of the energy dissipates in the current sheet within the light cylinder. We applied this result to PSR-B in PSR J0737-3039 and reestimate its surface magnetic field strength as $(7.3 \pm 0.2) \times 10^{11}$ G. Considering the orbital variability of the wind standoff distance, we estimate that the detected $\dot{P}$ of PSR-B likely shows a maximum time modulation of approximately $|\Delta \dot{P}_B|/\dot{P}_B \sim 4\%$, consistent with the uncertainties reported by Lyne et al. (2004). The lowest expected braking index of PSR-B is $n = 2.56$, based on our fitting formula for the spindown luminosity of aligned rotators confined with $R_m/R_{LC} \lesssim 1$. We speculate that the toroidal twist found in strongly compressed magnetospheres with $R_m/R_{LC} = 1/3$ can increase the plasma multiplicity in the closed zone of PSR-B and thereby produce the observed radio eclipse (see Lyutikov & Thompson 2005). The work presented in this paper is a stepping stone for improved predictions of observables such as the braking index and the time modulation of $\dot{P}$ as a function of χ and the magnetospheric confinement parameter R_m/R_{LC}. We will validate our predictions with further observations as PSR-B precesses back into our line of sight. In essence, our models advance our understanding of the spindown of PSR J0737-3039 while also providing insights into future observations of closely interacting NS binaries.

Acknowledgments

This research was facilitated by the Multimessenger Plasma Physics Center (MPPC, NSF grant PHY-2206607) and the Simons Foundation grant MP-SCMPS-00001470. Y.Z. is supported by JSPS Grants-in-Aid for Scientific Research No. JP23KJ0392 and the International Graduate Program for Excellence in Earth-Space Science (IGPEES). J.F.M. acknowledges support of DOE grant DE-SC0023015 and NSF grant AST-1909458. The computing resources were provided and supported by Princeton Research Computing.

Appendix
Kelvin–Helmholtz Instability at the Magnetopause

We note that Kelvin–Helmholtz instability generally forms at the pulsar magnetopause in our wind-magnetosphere simulations (see the inset of Figure 1 and also the white dotted rectangles in Figure 7), which is expected to be an extra source of dissipation. These vortices are closely connected to the wind plasma leaking into the pulsar magnetosphere, as shown in Figure 7. This can be regarded as an analogy to the transport of solar wind at the Earth's magnetopause via the formation of Kelvin–Helmholtz vortices (e.g., Hasegawa et al. 2004). Though minor in the parameter regime we are investigating, the interchange of plasma at the magnetopause can effectively change the particle composition in the pulsar magnetosphere, and may have nontrivial imprints on the nonthermal spectrum of the particles from this layer.

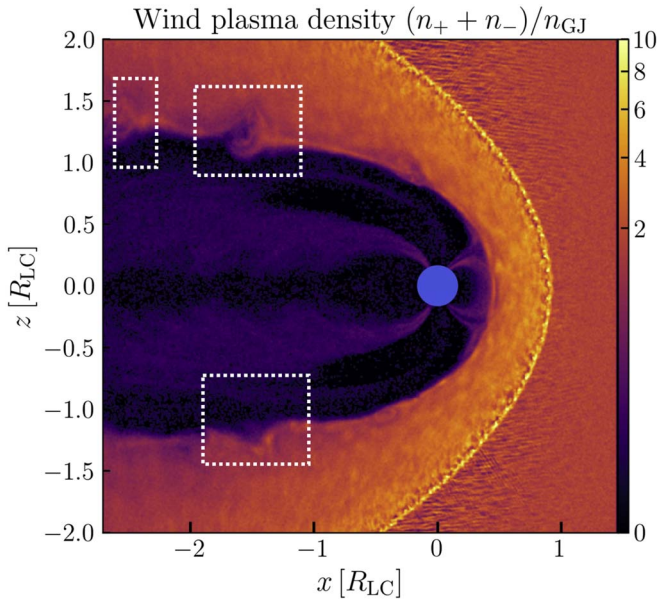

Figure 7. Mixing of plasma from the wind and pulsar magnetosphere at the same moment as Figure 1. We show a slice of wind plasma density when the pulsar magnetosphere with $R_{\rm LC}/R_* = 6$ is confined by $R_{\rm m}/R_{\rm LC} = 1/2$, in the $y = 0$ plane. Kelvin–Helmholtz instability develops in various locations of the pulsar magnetopause (white dotted rectangles).

ORCID iDs

Yici Zhong https://orcid.org/0000-0003-0805-8234
Anatoly Spitkovsky https://orcid.org/0000-0001-9179-9054
Jens F. Mahlmann https://orcid.org/0000-0002-5349-7116
Hayk Hakobyan https://orcid.org/0000-0001-8939-6862

References

Arons, J., Backer, D. C., Spitkovsky, A., & Kaspi, V. M. 2005, in ASP Conf. Ser. 328, Binary Radio Pulsars, ed. F. A. Rasio & I. H. Stairs (San Francisco, CA: ASP), 95
Axford, W. I. 1962, JGR, 67, 3791
Breton, R. P., Kaspi, V. M., Kramer, M., et al. 2008, Sci, 321, 104
Burgay, M., D'Amico, N., Possenti, A., et al. 2003, Natur, 426, 531
Carrasco, F., Palenzuela, C., & Reula, O. 2018, PhRvD, 98, 023010
Cerutti, B., Philippov, A. A., & Dubus, G. 2020, A&A, 642, A204
Cerutti, B., Philippov, A. A., & Spitkovsky, A. 2016, MNRAS, 457, 2401
Chen, A. Y., & Beloborodov, A. M. 2014, ApJL, 795, L22
Chen, Y.-W., Shue, J.-H., Zhong, J., & Shen, H.-W. 2023, ApJ, 957, 26
Contopoulos, I. 2005, A&A, 442, 579
Contopoulos, I., Kazanas, D., & Fendt, C. 1999, ApJ, 511, 351
Cortés, J., & Sironi, L. 2022, ApJ, 933, 140
Crawford, F., Lyne, A. G., Stairs, I. H., et al. 2013, ApJ, 776, 20
Cruz, F., Grismayer, T., Chen, A. Y., et al. 2023, A&A, in press
Demorest, P., Ramachandran, R., Backer, D. C., et al. 2004, ApJL, 615, L137
Fruchter, A. S., Stinebring, D. R., & Taylor, J. H. 1988, Natur, 333, 237
Ganguli, G., Crabtree, C., Fletcher, A., & Amatucci, B. 2020, RvMPP, 4, 12
Goldreich, P., & Julian, W. H. 1969, ApJ, 157, 869
Gruzinov, A. 2005, PhRvL, 94, 021101
Hakobyan, H., Philippov, A., & Spitkovsky, A. 2023, ApJ, 943, 105
Hasegawa, H., Fujimoto, M., Phan, T. D., et al. 2004, Natur, 430, 755
Hewish, A., Bell, S. J., Pilkington, J. D. H., Scott, P. F., & Collins, R. A. 1968, Natur, 217, 709
Hu, R., & Beloborodov, A. M. 2022, ApJ, 939, 42
Jackson, J. D. 1975, Classical Electrodynamics (New York: Wiley)
Kaspi, V. M., & Helfand, D. J. 2002, in ASP Conf. Ser. 271, Neutron Stars in Supernova Remnants, ed. P. O. Slane & B. M. Gaensler (San Francisco, CA: ASP), 3
Kramer, M., Stairs, I. H., Manchester, R. N., et al. 2006, Sci, 314, 97
Livingstone, M. A., Kaspi, V. M., Gavriil, F. P., et al. 2007, Ap&SS, 308, 317
Lyne, A. G., Burgay, M., Kramer, M., et al. 2004, Sci, 303, 1153
Lyutikov, M. 2004, MNRAS, 353, 1095
Lyutikov, M., & Thompson, C. 2005, ApJ, 634, 1223
Magalhaes, N. S., Miranda, T. A., & Frajuca, C. 2012, ApJ, 755, 54
McLaughlin, M. A., Kramer, M., Lyne, A. G., et al. 2004, ApJL, 613, L57
Michel, F. C. 1973, ApJL, 180, L133
Ostriker, J. P., & Gunn, J. E. 1969, ApJ, 157, 1395
Perera, B. B. P., Kim, C., McLaughlin, M. A., et al. 2014, ApJ, 787, 51
Pétri, J. 2015, MNRAS, 455, 3779
Philippov, A. A., & Spitkovsky, A. 2014, ApJL, 785, L33
Philippov, A. A., & Spitkovsky, A. 2018, ApJ, 855, 94
Philippov, A. A., Spitkovsky, A., & Cerutti, B. 2015, ApJL, 801, L19
Ruiz, M., Paschalidis, V., & Shapiro, S. L. 2014, PhRvD, 89, 084045
Russell, C., Le, G., Chi, P., et al. 2000, AdSpR, 25, 1369
Scharlemann, E. T., & Wagoner, R. V. 1973, ApJ, 182, 951
Shue, J. H., Chao, J. K., Fu, H. C., et al. 1997, JGR, 102, 9497
Sironi, L., & Spitkovsky, A. 2011, ApJ, 741, 39
Soudais, A., Cerutti, B., & Contopoulos, I. 2024, A&A, in press
Spitkovsky, A. 2005, in AIP Conf. Ser. 801, Astrophysical Sources of High Energy Particles and Radiation, ed. T. Bulik, B. Rudak, & G. Madejski (Melville, NY: AIP), 345
Spitkovsky, A. 2006, ApJL, 648, L51
Timokhin, A. N. 2006, MNRAS, 368, 1055
Timokhin, A. N., & Harding, A. K. 2019, ApJ, 871, 12
Werner, G. R., Uzdensky, D. A., Begelman, M. C., Cerutti, B., & Nalewajko, K. 2018, MNRAS, 473, 4840